scientific reports

Check for updates

OPEN

Two-dimensional boron nitride allotrope Irida-$B_{12}N_{12}$ with 3-6-8 membered rings and wide-bandgap semiconducting properties

Marcelo L. Pereira Jr[1]✉, Djardiel da S. Gomes[2], Kleuton A. L. Lima[3], Georges D. A. Nze[1], Fábio L. L. Mendonça[1] & Luiz A. Ribeiro Jr[3]

We present a novel two-dimensional (2D) boron nitride allotrope, Irida-$B_{12}N_{12}$ (Ir-BN), analogous to the all-carbon Irida-Graphene (Ir-G). The predicted structure of Ir-BN consists of alternating boron and nitrogen atoms, forming three distinct lattices with 3-, 6-, and 8-membered ring patterns. First-principles calculations based on density functional theory (DFT) formalism and ab initio molecular dynamics (AIMD) simulations were performed to investigate its structural, mechanical, electronic, and optical properties. The Ir-BN lattices exhibit good dynamical and thermal stability, supporting their viability as new 2D materials. Substantial anisotropy is observed in the mechanical properties, with in-plane stiffness ranging from 16 to 142 N/m, depending on the direction, and bulk moduli between 78 and 95 N/m. The electronic structure analysis reveals that Ir-BN is a wide-bandgap semiconductor, with band gaps ranging from 2.4 to 3.2 eV. The material shows optical activity particularly in the visible and ultraviolet regions.

Keywords Two-dimensional Systems, Boron-Nitride Materials, Physical Properties, Density Functional Theory

The continuous development of 2D materials has significantly advanced our understanding of nanomaterials and their potential applications in modern technology[1]. Since synthesizing graphene in 2004[2], interest in other 2D materials has increased significantly[3], driven by the need to discover new materials that exhibit unconventional properties not present in their bulk counterparts with a lower surface-to-volume ratio[4]. Among these 2D materials, boron nitride-based structures have emerged as significant contenders, especially in nanoelectronics, due to their mechanical and thermal stability and wide-bandgap semiconducting behavior[5].

In its 2D form, boron nitride is often called hexagonal boron nitride (h-BN)[6]. It is structurally analogous to graphene but has alternating boron and nitrogen atoms in a honeycomb lattice. This material has been widely studied for its electrical insulating properties[7], making it a valuable component in heterostructures and devices[8]. However, the quest for novel 2D boron nitride allotropes that exhibit diverse and tunable properties remains critical[9]. Such allotropes could open new avenues for applications in fields ranging from optoelectronics to energy storage[10].

Two-dimensional boron nitride materials offer various structural possibilities, paralleling the variety found in carbon-based materials[7,11,12]. For example, h-BN[13], amorphous BN monolayers[14], penta-BN[15], T-BN[16], octagonal-BN[17], PAI-BN[18], DHQ-BN[19], g-B_3N_5[20], and Ψ-BN[21]exhibit distinct atomic arrangements, each contributing unique properties to the landscape of novel nanomaterials. Exploring PHA-Graphene and PHA-BN has also extended the boundaries of 2D boron nitride structures[22–24]. The boron nitride analog of the Biphenylene Network (BPN), BPN-BN[12,25], has garnered particular attention due to its intriguing properties and the recent synthesis of the all-carbon BPN[26].

Recent advancements in computational materials design have led to the prediction of 2D carbon allotropes with novel ring patterns[27],. Among them, Ir-G[28], is characterized by an intricate lattice composed of 3-, 6-, and 8-membered rings that impart interesting electronic and mechanical properties, which have been studied for various possible applications and variations[29–36]. Inspired by this structure, we propose a boron nitride analog, Irida-BN (Ir-BN), which retains the alternating boron and nitrogen atoms while adopting the 3–6-8 ring

[1]University of Brasília, College of Technology, Department of Electrical Engineering, Brasília, Brazil. [2]University of Brasília, Faculty UnB Planaltina, Materials Science Postgraduate Program, Brasília, Brazil. [3]University of Brasília, Institute of Physics, Brasília, Brazil. ✉email: marcelo.lopes@unb.br

arrangement. The prediction and characterization of Ir-BN contribute to the expanding field of 2D materials, particularly boron nitride allotropes[11]. Our findings provide insights into this novel material's potential and lay the groundwork for future experimental validation and exploration.

This study employs DFT calculations and AIMD simulations to predict Ir-BN's mechanical, structural, electronic, and optical properties. The predicted structure of Ir-BN consists of alternating boron and nitrogen atoms, forming three distinct lattices with unique 3–6-8 membered ring patterns. By analyzing this allotrope's stability and potential functionality, we aim to understand its characteristics comprehensively. Our results indicate that the Ir-BN lattices exhibit good dynamical and thermal stability, a wide bandgap ranging from 2.4 to 3.2 eV, and pronounced anisotropy in their mechanical properties, with in-plane stiffness ranging from 16 to 142 N/m. Additionally, the optical activity of Ir-BN is significant in the visible and ultraviolet regions, suggesting promising applications in optoelectronics.

Results and discuss

Structural and stability properties

To begin our discussion on the structural features of Ir-BN, Figure 1 presents the three distinct Ir-BN lattices proposed in this study: (a) Ir-BN^A (hex-B_4N_2), (b) Ir-BN^B (hex-B_2N_4), and (c) Ir-BN^C (hex-B_3N_3). These lattices, containing 24 atoms in their unit cells, were initially optimized using the PBE method. The unit cell of each lattice was designed based on variations of the hexagonal ring (hex-), as previously mentioned. The Ir-BN^A lattice has lattice vectors of 11.78 Å and 6.63 Å, with its hexagons consisting of four boron atoms paired with two nitrogen atoms. The Ir-BN^B lattice features lattice vectors of 11.15 Å and 6.78 Å, with reversed hexagonal rings compared to Ir-BN^A, consisting of four nitrogen atoms paired with two boron atoms. Finally, the Ir-BN^C lattice shows lattice vectors of 11.13 Å and 6.75 Å, with hexagonal rings interspersed between B and N, with no paired atoms in this case. In all lattices, starting from the hexagon design, bonds were constructed by intercalating nitrogen and boron atoms. In the Ir-BN^A lattice, triangular rings feature two nitrogen atoms for every boron atom, while in the Ir-BN^B lattice, the triangles contain two boron atoms for every nitrogen atom. The Ir-BN^C lattice has half of the triangles with more nitrogen than boron and the other half with more boron than nitrogen. All lattices have lattice angles of $\alpha = \beta = \gamma = 90^\circ$, corresponding to the space group CMMM (D2H-19). These lattices exhibit a ring structure of 3, 6, and 8 boron and nitrogen atoms. The variations in topology result in distinct electronic and structural characteristics, which are detailed subsequently. See supplementary information to crystal information data.

The bond distances for B-N, B-B, and N-N differ based on the system's atomic arrangement. In phase A of Ir-BN, the 3-membered BN-ring exhibits N-N bonds of 1.76 Å and B-N bonds of 1.43 Å. B-B bonds are 1.71 Å in the hexagonal rings, and B-N bonds are 1.50 Å. The B-N bond between triangular (via B) and hexagonal (via N) rings measures 1.45 Å, while the B-N bond between triangular (via N) and hexagonal (via B) rings is 1.42 Å. In Ir-BN^B, the B-B and B-N bonds in the triangular rings are 1.60 Å and 1.42 Å, respectively. The N-N and B-N bonds in the hexagonal rings are 1.62 Å and 1.45 Å, respectively. The B-N bond between boron in the 6-membered BN-ring and nitrogen in the 3-membered BN-ring is 1.48 Å, whereas, for nitrogen in the hexagonal and boron in the triangular rings, it is 1.43 Å. Lastly, in Ir-BN^C, the B-N bonds in the hexagonal rings vary slightly around 1.48 Å. In the 3-membered BN-ring, the B-B, N-N, and B-N bonds are 1.58 Å, 1.83 Å, and 1.42 Å, respectively. The remaining B-N bonds in the octagonal rings are approximately 1.44 Å. Notably, the bond distances in this table are also present in other 2D boron nitride allotropes[6,15,21].

After discussing the lowest energy configurations obtained for the three phases of Ir-BN investigated here, we also calculated the cohesion energy in all cases using the expression

$$E_{\mathrm{coh}} = \frac{1}{24} E_{\text{Ir-BN}} - \frac{1}{2}(E_{\mathrm{B}} + E_{\mathrm{N}}), \tag{1}$$

where $E_{\text{Ir-BN}}$ is the total energy of Ir-BN, and E_{B} and E_{N} are the energies of isolated B and N atoms, respectively. We obtained −9.72 eV/atom, −9.21 eV/atom, and −9.50 eV/atom for Ir-BN^A, Ir-BN^B, and Ir-BN^C

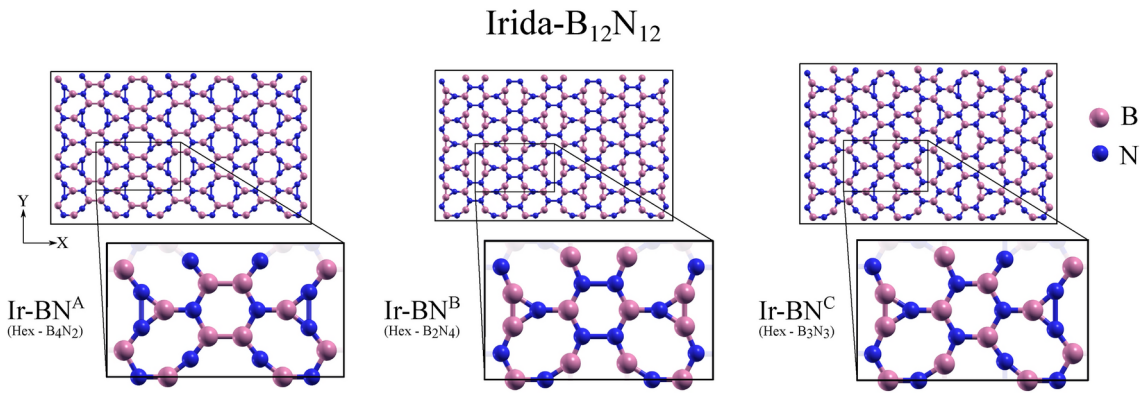

Fig. 1. Schematic representation of the Ir-BN lattices. The black lines highlight their unit cells and lattice vectors.

, respectively. Using the same method, we calculated the cohesion energy of h-BN (adjusted for the differences in the expression for E_{coh}), which is −8.72 eV/atom. These values are consistent with those found for other two-dimensional boron nitride allotropes, such as DHQ-BN (−7.71eV/atom)[19] and Ψ-BN (−7.48eV/atom)[21], as well as with the range presented in the literature for h-BN (both pristine and defective) between −9.0 eV/atom to −4.0eV/atom[37,38]. It is important to note that the best quantitative comparison is made when calculations are performed using the same methodology. However, we demonstrate here that the Ir-BN systems are energetically stable.

After optimizing and confirming the energetic stability of the systems investigated, as discussed above, the mechanical stability of the three Ir-BN variants was assessed through phonon dispersion calculations, which detect vibrational modes with imaginary frequencies, indicating dynamic instability. These calculations were performed on a $3 \times 3 \times 1$ supercell with a mesh cutoff of 800 Ry to interpolate the phonon modes. The convergence criteria were set with an energy threshold of 10^{-5} eV and a force threshold of 0.001 eV/Å. The acoustic sum rule was also applied at the Γ point to eliminate any artificial imaginary frequencies. The phonon spectra for the Ir-BN lattices are shown in Figure 2. The spectra confirm the vibrational stability of Ir-BN^A, Ir-BN^B, and Ir-BN^C, with no negative frequencies observed, indicating that these lattices are dynamically stable. The highest frequencies observed are 1695 cm^{-1} for Ir-BN^A, 1646 cm^{-1} for Ir-BN^B, and 1695 cm^{-1} for Ir-BN^C. In all three systems, there are three acoustic modes: flexural (ZA), transverse (TA), and longitudinal (LA). In the case of Ir-BN^A, the LA and TA dispersions coincide, unlike Ir-BN^B and Ir-BN^C, which exhibit different dispersions in the acoustic modes. Generally, the phonon dispersions of Ir-BN are similar across all systems due to the uniform density of B-B, N-N, and B-N bonds. Another common feature among the three systems is the absence of a significant gap between the acoustic and optical branches in the phonon spectra, suggesting considerable phonon scattering within these materials. This trend implies frequent phonon interactions, which could contribute to lower thermal conductivity in Ir-BN lattices.

After investigating the energetic and dynamic stability of Irida-B_{12} N_{12}, we also calculated the system dynamics in the presence of temperature. The thermal stability of the Ir-BN lattices was verified through AIMD simulations at 300 K, as shown in Figure 3. We used supercells of $1 \times 2 \times 1$ with 48 atoms for these simulations. The AIMD calculations employed a time step of 0.5 fs, using an isobaric-isothermal ensemble, keeping pressure, number of atoms, and temperature constant (NPT). The pressure (set to zero) was controlled using a Parrinello-Rahman barostat, and the temperature was regulated by a Nosé-Hoover thermostat. Figures 3(a,b), 3(c,d), and 3(e,f) show the time evolution of the total energy and temperature for the Ir-BN^A, Ir-BN^B, and Ir-BN^C lattices, respectively. The insets in the panels display the top and side views of the final AIMD snapshots at eight ps. These figures show that the total energy remains stable and flat throughout the simulations for all lattices, indicating no significant lattice reconfiguration occurs. The insets reveal the absence of bond-breaking or structural reconstruction.

While Ir-BN^B exhibits a flat structure (see Figure 3(b)), Ir-BN^A and Ir-BN^C (see Figures 3(a) and 3(c)) show a slight curvature due to weaker N-N bonding interactions within the triangular rings of the system. These results demonstrate that Ir-BN^A, Ir-BN^B, and Ir-BN^C maintain good thermal stability under the simulated conditions. The rippling in these figures results from the simulated systems' inherent structural relaxation (intrinsic stress). This phenomenon is consistent with other studies of 2D materials, where out-of-plane distortions occur due to residual stress. The distinct ring topology of Ir-BN, particularly the 3-membered ring, imposes B-N bond patterns that yield these out-of-plane distortions.

Regarding the structure's size, rippling may become more pronounced or evolve differently in larger systems. However, in preliminary simulations using more significant supercells, we observed that while the rippling persists, the overall amplitude remains on the same order of magnitude, suggesting that it is a localized effect rather than one that scales dramatically with system size. The absence of rippling signatures in the phonon spectrum can be attributed to phonon spectra reflecting the vibrational modes of the material in its equilibrium

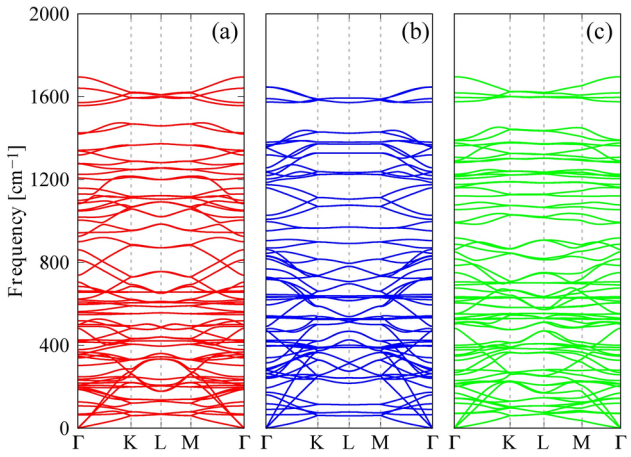

Fig. 2. Phonon dispersion curves for (**a**) Ir-BN^A, (**b**) Ir-BN^B, and (**c**) Ir-BN^C.

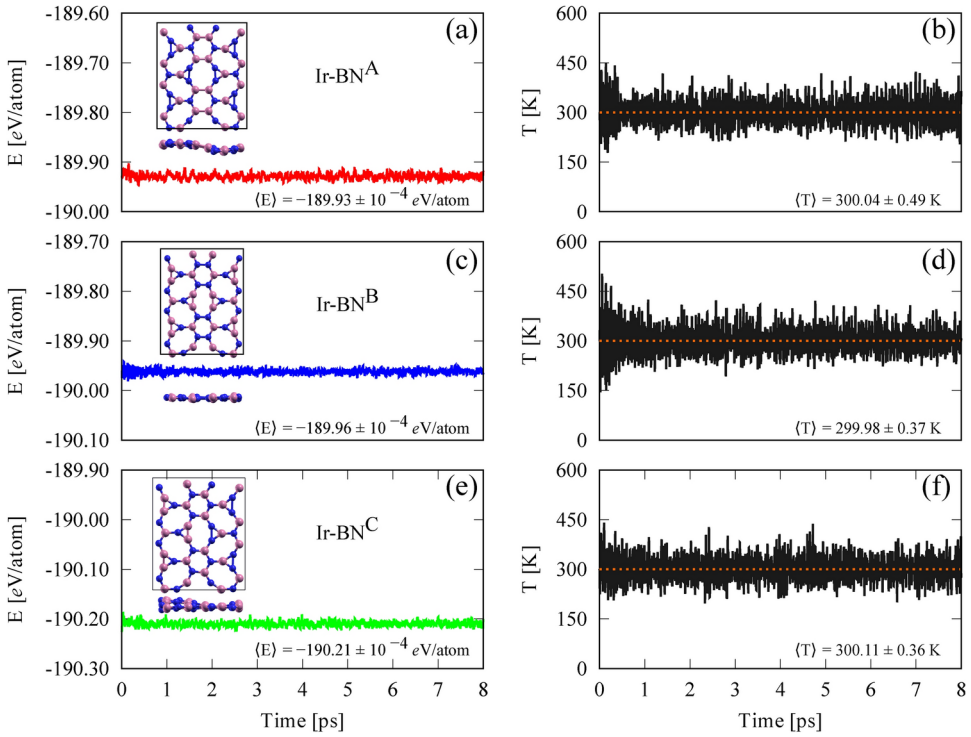

Fig. 3. Time evolution of the total energy per atom for Ir-BN lattices at 300K, during 8 ps of simulation. The inset figures show the top and side views for the final AIMD snapshots.

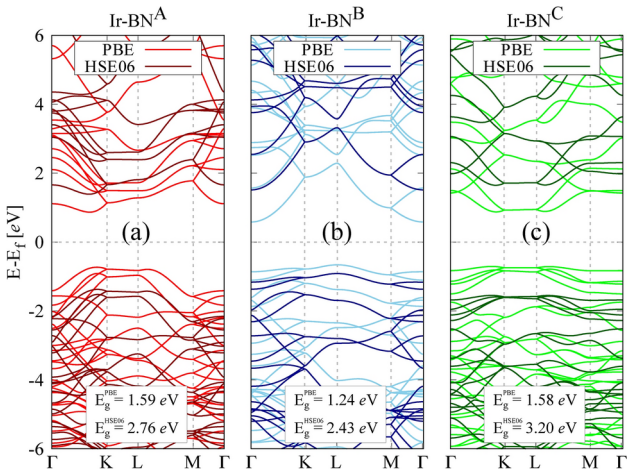

Fig. 4. Electronic band structure for (**a**) Ir-BN^A, (**b**) Ir-BN^B, and (**c**) Ir-BN^C calculated using the PBE and HSE06 approaches.

configuration at 0 K. The rippling in our system arises from static structural deformations rather than dynamic phonon modes. Thus, the phonon spectrum would not show a direct signature of these ripples, which are more likely a result of geometric relaxation rather than vibrational instabilities.

Finally, we evaluated the thermal stability of the Ir-BN structures at different temperatures – 500 K, 750 K, and 1000 K – using the same methodology. All systems were stable at 500 K. Ir-BN^B, and Ir-BN^C exhibited structural stability up to 1000 K and 750 K, respectively. In this way, all the Ir-BN systems have good thermal stability at temperatures higher than room temperature.

Electronic properties

We now discuss the electronic band structure of the Ir-BN lattices, as depicted in Figure 4. The band structures were calculated using the PBE and HSE06. For Ir-BN^A, Ir-BN^B, and Ir-BN^C, the PBE/HSE06 band gaps are 1.59/2.76 eV, 1.24/2.43 eV, and 1.58/3.20 eV, respectively. As is well-known, the PBE method generally

underestimates band gaps, making the HSE06 approach essential for accurate electronic characterization. According to the HSE06 results, these materials are wide-band gap semiconductors. These band gap values are lower than the band gap of hBN, which is approximately 5.68 eV as reported in the Computational 2D Materials Database (C2DB)[39].

In Ir-BN^A and Ir-BN^B, more N-N and B-B bonds reduce the band gap regarding the Ir-BN^C case. These bonds, having lower strengths compared to the B-N bonds, introduce additional energy levels within the band structure, which can lead to narrower band gaps. Additionally, the ring structure within the Ir-BN lattices plays a significant role in shaping their band structures. Specifically, the 3-atom rings in these materials create shorter bonds with more substantial orbital overlap than the B-N bonds in conventional h-BN. This increased overlap facilitates greater electron delocalization, extending the electronic states within the band structure and consequently leading to a reduced band gap.

Figures 5(a), 5(b), and 5(c) display the total density of states (DOS) for the Ir-BN^A, Ir-BN^B, and Ir-BN^C lattices, respectively. The DOS plots highlight the band gaps observed in these materials, consistent with the results shown in Figure 4. Figures 5(d), 5(e), and 5(f) present the partial density of states (PDOS) for Ir-BN^A, Ir-BN^B, and Ir-BN^C calculated using the PBE method. This analysis reveals that the p-orbitals of boron (B^{2p}) and nitrogen (N^{2p}) significantly contribute to the density of states, with B^{2p} orbitals mainly populating the conduction band and N^{2p} orbitals dominating the valence band. In all cases, the smearing parameter used was 0.15 eV.

Figures 5(g), 5(h), and 5(i) show the PDOS results calculated with the HSE06 functional. The HSE06 results confirm the trends observed with PBE, with B^{2p} and N^{2p} orbitals continuing to play crucial roles in the electronic structure. The prominence of N^{2p} orbitals in the valence band and B^{2p} orbitals in the conduction band underscores their importance in the electronic transitions and interactions within these lattices. They are often associated with directional bonding phenomena.

The HSE06 functional typically provides more accurate bandgaps than PBE. However, in some cases, the HSE06 functional may underestimate the CBM compared to the PBE. There are a few plausible reasons why this happens: screened exchange in HSE06 is used to treat short-range interactions with Hartree-Fock exchange and long-range interactions with PBE exchange; the screening parameter in HSE06 may also influence the position of the CBM, i.e., it may shift the CBM downwards, leading to an underestimation compared to the PBE. The inclusion of Hartree-Fock exchange in HSE06 affects orbital energies, especially for unoccupied states such as the CBM, which leads to an improved description of the valence band and the overall band gap. Unoccupied states may be more sensitive to Hartree-Fock exchange, leading to a lower CBM in some materials; the PBE functional suffers from a higher degree of self-interaction error, which may artificially inflate the CBM energy. HSE06, which partially corrects for self-interaction, results in a lower CBM. However, it often provides a more realistic description of unoccupied states and material-dependent effects, where the degree to which HSE06 shifts the CBM compared to the PBE can vary depending on the material's electronic structure. In some semiconductors, for example, the CBM may be dominated by specific orbitals more affected by the Hartree-Fock exchange, leading to a more significant shift relative to the PBE.

Further insights into the electronic properties of the Ir-BN lattices are obtained through the analysis of the highest occupied crystal orbital (HOCO), lowest unoccupied crystal orbital (LUCO), and electron localization

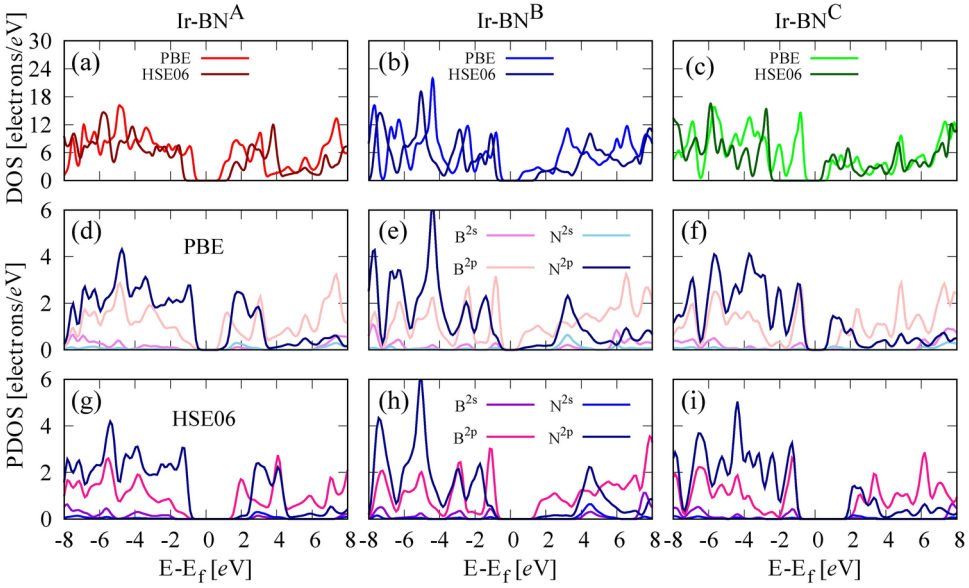

Fig. 5. Total density of states (DOS) for (**a**) Ir-BN^A, (**b**) Ir-BN^B, and (**c**) Ir-BN^C lattices. The partial density of states (PDOS) calculated using the PBE approach is presented in panels (**d**), (**e**), and (**f**) for the Ir-BN^A, Ir-BN^B, and Ir-BN^C lattices. The PDOS results obtained at the HSE06 level for Ir-BN^A, Ir-BN^B, and Ir-BN^C lattices are depicted in panels (**g**), (**h**), and (**I**), respectively.

function (ELF), as shown in Figure 6. These analyses provide a deeper understanding of the chemical interactions within the lattices.

In the left-most column of Figure 6, one can note that the HOCO for Ir-BN^A, Ir-BN^B, and Ir-BN^C predominantly localizes on the nitrogen atoms within the rings. In contrast, the LUCO is centered in all atoms, as shown in the central column. This pattern is consistent across all three lattices, highlighting a tendency for nitrogen atoms to host both HOCO and LUCO and boron atoms to accommodate the LUCO. This behavior is reflected in the ELF analysis as well. The ELF values in the right-most column of Figure 6 demonstrate a high degree of electron localization around the nitrogen atoms, indicating strong interactions or lone pair electrons associated with these atoms. In contrast, boron atoms exhibit lower ELF values, suggesting a more delocalized electronic distribution.

The observed differences in the HOCO and LUCO distributions are due to the electronegativity disparity between boron and nitrogen atoms. Nitrogen, being more electronegative, attracts the electron density, leading to the observed localization of the LUCO on boron atoms. This trend is corroborated by the ELF analysis, which illustrates localized electron density around nitrogen and more delocalized regions around boron. This is also consistent with the electronic structure observed in the band structure analysis.

Optical properties

Figure 7 delves into the optical properties of the Ir-BN^A, Ir-BN^B, and Ir-BN^C lattices, focusing on light polarization along the x (100), y (010), and z (001) directions. In this figure, the top, central, and bottom rows illustrate the absorption coefficient, refractive index, and reflectivity as a function of the photon energy. These optical properties were computed using the HSE06 method. The optical calculations apply a constant external electric field with an intensity of 1.0 V/Å along the x, y, and $z$directions (separately). We use Fermi's golden rule[40]and the Kramers-Kronig relation[41,42] to calculate the real (ϵ_1) and imaginary (ϵ_2) parts of the dielectric constant (see support information Fig. S1 to Ir-BN). From this methodology, (ϵ_1) is obtained through the expression

$$\epsilon_1(\omega) = 1 + \frac{1}{\pi} P \int_0^\infty d\omega' \frac{\omega' \epsilon_2(\omega')}{\omega'^2 - \omega^2} \quad , \tag{2}$$

where P denotes the principal value of the integral over ω'. The imaginary part, which considers interband optical transitions between the valence band (VB) and the conduction band (CB), is expressed as:

$$\epsilon_2(\omega) = \frac{4\pi^2}{\Omega\omega^2} \sum_{\substack{i \in \mathrm{VB} \\ j \in \mathrm{CB}}} \sum_k W_k \left|\rho_{ij}\right|^2 \delta(\epsilon_{kj} - \epsilon_{ki} - \hbar\omega) \ , \tag{3}$$

In this equation, ω represents the photon frequency, $|\rho_{ij}|$ is the dipole transition matrix element, and W_k is the weight of the respective k-point in the reciprocal space. Additionally, Ω is the system volume. Through ϵ_1 and ϵ_2, it is possible to determine other properties presented on figure 7, such as the absorption coefficient (α), reflectance (R), and refractive index (η):

$$\alpha(\omega) = \omega \sqrt{2 \left[\sqrt{\epsilon_1^2(\omega) + \epsilon_2^2(\omega)} - \epsilon_1(\omega) \right]}, \tag{4}$$

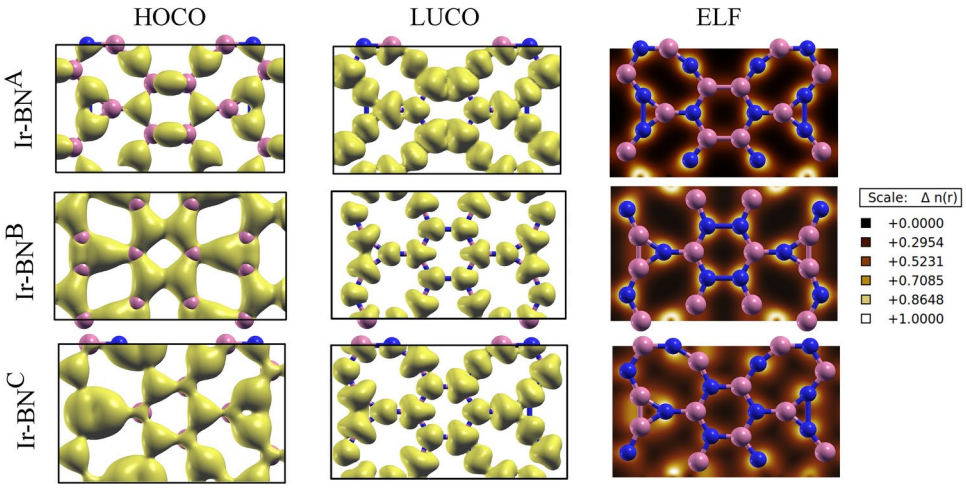

Fig. 6. The left-most, central, and right-most columns show the HOCO, LUCO, and ELF results for the Ir-BN lattices.

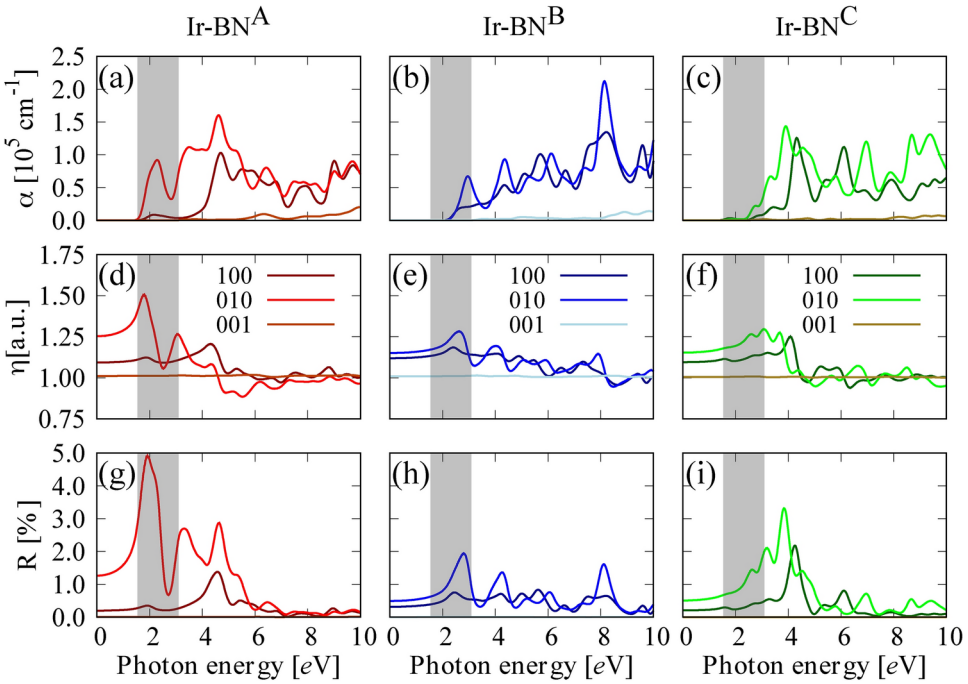

Fig. 7. The top, central, and bottom rows illustrate the absorption coefficient, refractive index, and reflectivity as a function of the photon energy for the Ir-BN latices.

$$R(\omega) = \left[\frac{\sqrt{\epsilon_1(\omega) + i\epsilon_2(\omega)} - 1}{\sqrt{\epsilon_1(\omega) + i\epsilon_2(\omega)} + 1}\right]^2, \text{ and} \tag{5}$$

$$\eta(\omega) = \frac{\sqrt{2}}{2}\left[\sqrt{\epsilon_1^2(\omega) + \epsilon_2^2(\omega)} + \epsilon_1(\omega)\right]^2. \tag{6}$$

Overall, the optical activity of Ir-BN^A (Figure 7(a,d,g)), Ir-BN^B (Figure 7(b,e,h)), and Ir-BN^C (Figure 7(c,f,i)) is intense in the visible and ultraviolet regions. This characteristic aligns with their observed band gaps. This behavior is consistent with other 2D boron nitride materials. The pronounced optical activity across this range indicates that these lattices could be effectively utilized in UV-Vis-based applications.

The optical absorption spectra for Ir-BN^A, Ir-BN^B, and Ir-BN^C, shown in Figures 7(a,b,c), reveal substantial absorption primarily in the UV region. This trend suggests that these materials could be advantageous as UV collectors. The high refractive index values for Ir-BN^A, Ir-BN^B, and Ir-BN^C, illustrated in Figures 7(d,e,f), suggest strong polarization capabilities in response to external electric fields. Additionally, the low reflectivity for Ir-BN^A, Ir-BN^B, and Ir-BN^C observed in Figures 7(g,h,i) is restricted to the UV range, underscoring their utility in UV applications. Ir-BN^A is also a good visible light reflector.

Mechanical properties

For a more comprehensive characterization of the Irida-B_{12} N_{12} phases investigated here, we calculated key parameters such as in-plane stiffness (C), bulk modulus (B), and Poisson's ratio (ν). For this analysis, we used a supercell ($1 \times 2 \times 1$) oriented in the xy plane and applied tensile strain independently in the x, y, and xy directions. For uniaxial strain, the lattice constants a and b were incrementally varied by 0.5% up to the end of the material's plastic region, starting from their optimized values. The system's total energy was computed at each deformation step. The in-plane stiffness, C, is given by[43,44]

$$C = \frac{1}{A} \times \left(\frac{\partial^2 E_S}{\partial \varepsilon^2}\right)\Big|_{\varepsilon=0}, \tag{7}$$

where A is the area of the optimized supercell, ε denotes the uniaxial strain defined as $\varepsilon = \Delta l/l_0$ (with l_0 being the initial length of the supercell and $\Delta l = l - l_0$ the change in length upon straining), and E_S represents the strain energy, calculated by subtracting the equilibrium total energy from the total energy at each strain point.

The in-plane bulk modulus, B, quantifies the material's response to area deformation and is computed as the second derivative of the strain energy concerning the area of the 2D structure

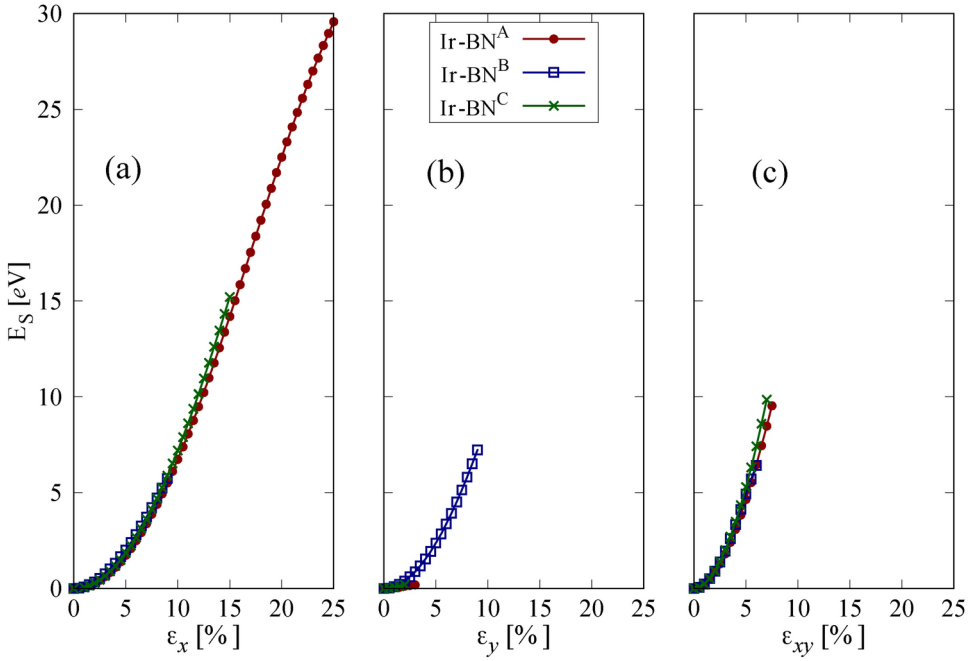

Fig. 8. Stress-strain relationships of Ir-BN lattices under (**a**) uniaxial tensile loading in the *x*-direction, (**b**) *y*-direction, and (**c**) biaxial tensile loading.

Ir-BN	*x*-direction strain			*y*-direction strain			*xy*-direction strain	
	C (N/m)	ϵ (%)	ν (arb. units)	C (N/m)	ϵ (%)	ν (arb. units)	B (N/m)	ϵ (%)
Ir-BN^A	107.8	25.0	0.64	16.6	3.5	0.51	79.0	7.5
Ir-BN^B	135.9	8.0	0.19	17.1	9.5	0.20	91.2	6.0
Ir-BN^C	142.0	15.5	0.47	54.8	2.0	0.54	95.0	7.0

Table 1. Elastic properties of the Ir-BN material under different strain directions. The table presents the elastic modulus (C), maximum strain (ϵ), and Poisson's ratio (ν) in the x and y directions, as well as the shear modulus (B) and the corresponding strain in the xy direction.

$$B = A \times \left(\frac{\partial^2 E_S}{\partial A^2} \right) \Bigg|_{A_0}, \tag{8}$$

where A_0 and Arepresent the unit cell area in equilibrium and after strain application, respectively[45,46].

Poisson's ratio, ν, measures the ratio of transverse strain to axial strain for small deformations and is given by[47]:

$$\nu = -\frac{\varepsilon_{\text{trans}}}{\varepsilon_{\text{axial}}}. \tag{9}$$

In this perspective, we examined the mechanical properties of the Ir-BN^A, Ir-BN^B, and Ir-BN^C lattices through uniaxial and biaxial tensile tests. These tests provide insights into the structural integrity and resilience of these materials. Figures 8(a) and 8(b) present the energy-strain relationships for tensile loading along the x and y directions, while Figure 8(c) illustrates the case for biaxial strain. The red, blue, and green curves denote this interplay for Ir-BN^A, Ir-BN^B, and Ir-BN^C, shown up to their critical strain (ε_C), i.e., the point just before the material's rupture. For all three lattices, the energy-strain curves indicate that the tensile forces remain within the limits of the lattice's bond strengths, preserving structural stability throughout deformation.

The data in Table 1 reveal notable anisotropy in mechanical behavior. The Ir-BN^A, Ir-BN^B, and Ir-BN^C lattices exhibit different responses to strain in the x and y directions, reflected in their respective in-plane stiffness values and elastic moduli (C). For example, the in-plane stiffness values of Ir-BN^A, Ir-BN^B, and Ir-BN^C differ. Elastic moduli in the x and y directions show a high degree of anisotropy, with values ranging from 16.56 to 141.97 N/m. These results suggest that the Ir-BN lattices' mechanical properties vary depending on the direction of

applied strain. Additionally, the Poisson's ratio (ν) values, calculated for a strain of 0.5%, highlight significant anisotropy in the deformation mechanisms of these materials. The Poisson's ratios in the x and y directions differ substantially, with values ranging from 0.20 to 0.64, indicating that the materials exhibit varying degrees of ductility along different crystallographic directions.

The biaxial strain tests underscore the mechanical behavior of Ir-BN^A, Ir-BN^B, and Ir-BN^C, with critical strains up to 7.0%. The calculated bulk moduli (B_M), which measure the materials' resistance to uniform compression, reflect their ability to withstand substantial biaxial strain without rapid failure (refer to Table 1). The values vary from 78.2 to 94.99 for the studied materials. The unique lattice topologies of Ir-BN^A, Ir-BN^B, and Ir-BN^C, characterized by their ring structures and bonding patterns, contribute to their distinct mechanical properties. The rigidity and flexibility observed in these lattices result from their distinct structural arrangements, which influence their overall mechanical performance.

In our study, the elastic properties were derived from energy versus strain curves, which allowed us to compute mechanical properties such as elastic modulus. However, we did not explicitly calculate the complete set of elastic constants to evaluate the mechanical stability criteria[48]. As discussed above, we employed phonon calculations and AIMD simulations, widely recognized as robust approaches for assessing the structural stability of materials. Based on the results from the simulations performed here, we did not observe any indications of structural instabilities in the IrBN systems.

Methods

The structural, electronic, optical, and mechanical properties of IrBN were investigated using the DFT formalism[49,50]implemented in the Spanish Initiative for Electronic Simulations with Thousands of Atoms (SIESTA) code[51,52]. The generalized gradient approximation (GGA) within the Perdew-Burke-Ernzerhof (PBE) functional was employed to describe the exchange-correlation potential[53]. Due to address the known limitations of GGA/PBE in underestimating the band gap, additional electronic structure calculations were conducted using the hybrid Heyd-Scuseria-Ernzerhof (HSE06) functional[54], with the HONPAS package[55,56]to obtain more accurate band gap values. Core-electron interactions were modeled using Troullier-Martins norm-conserving pseudopotentials[57,58] with a valence electron configuration of $2s^2$ and $2s^2\ 2p^3$ for boron and nitrogen atoms, repectively. We employed an energy cutoff of 800 Ry. A double-ζpolarized (DZP) basis set composed of finite-range numerical atomic orbitals was used. A Monkhorst-Pack[59] $50 \times 50 \times 1$ grid was applied to ensure accurate Brillouin zone sampling. The atomic positions and lattice vectors were optimized until the maximum force on each atom was less than 0.001 eV/Å, and the total energy difference was below 10^{-5} eV. A vacuum thickness of 30 Å was introduced along the out-of-plane direction to prevent spurious interactions between periodic images of the monolayer.

Conclusions

In summary, this study presents a detailed investigation of the structural, electronic, optical, and mechanical properties of Ir-BN^A, Ir-BN^B, and Ir-BN^C, highlighting their potential for various technological applications. The DFT calculations, including using both PBE and HSE06 functionals, confirm the stability of these novel 2D boron nitride allotropes and reveal their wide semiconducting band gaps, with band gap values ranging from 2.76 to 3.20 eV. The electronic structure analysis shows significant contributions from p-orbitals in valence and conduction bands, with bandgap values aligning well with those of similar materials, underscoring their potential use in optoelectronic devices.

The optical properties, particularly the pronounced UV absorption and low reflectivity, indicate that these materials could serve as effective UV collectors. Their high refractive index also suggests promising applications in photonics, where the ability to polarize light and interact with external electric fields is crucial. The distinct mechanical behavior of the Ir-BN^A, Ir-BN^B, and Ir-BN^C lattices, characterized by anisotropic responses to tensile strain, further demonstrates their suitability for applications requiring materials that combine strength, flexibility, and resilience under stress.

Data availability

The datasets utilized and/or examined throughout the present study are accessible upon reasonable request from the corresponding author.

Received: 19 September 2024; Accepted: 12 November 2024
Published online: 21 November 2024

References

1. Ares, P. & Novoselov, K. S. Recent advances in graphene and other 2d materials. *Nano Materials Science* **4**, 3–9 (2022).
2. Novoselov, K. S. *et al.* Electric field effect in atomically thin carbon films. *science* **306**, 666–669 (2004).
3. Rosenkranz, A., Liu, Y., Yang, L. & Chen, L. 2d nano-materials beyond graphene: from synthesis to tribological studies. *Applied Nanoscience* **10**, 3353–3388 (2020).
4. Si, J., Yu, J., Shen, Y., Zeng, M. & Fu, L. Elemental 2d materials: Progress and perspectives toward unconventional structures. *Small Structures* **2**, 2000101 (2021).
5. Angizi, S., Alem, S. A. A. & Pakdel, A. Towards integration of two-dimensional hexagonal boron nitride (2d h-bn) in energy conversion and storage devices. *Energies* **15**, 1162 (2022).
6. Zhang, K., Feng, Y., Wang, F., Yang, Z. & Wang, J. Two dimensional hexagonal boron nitride (2d-hbn): synthesis, properties and applications. *Journal of Materials Chemistry C* **5**, 11992–12022 (2017).
7. Roy, S. et al. Structure, properties and applications of two-dimensional hexagonal boron nitride. *Advanced Materials* **33**, 2101589 (2021).

8. Ren, J. & Innocenzi, P. 2d boron nitride heterostructures: recent advances and future challenges. *Small Structures* **2**, 2100068 (2021).
9. Wang, J., Zhang, L., Wang, L., Lei, W. & Wu, Z.-S. Two-dimensional boron nitride for electronics and energy applications. *Energy & Environmental Materials* **5**, 10–44 (2022).
10. Li, C. *et al.* Two dimensional borophene nanomaterials: Recent developments for novel renewable energy storage applications. *Progress in Solid State Chemistry* 100416 (2023).
11. Enyashin, A. & Ivanovskii, A. Graphene-like bn allotropes: Structural and electronic properties from dftb calculations. *Chemical Physics Letters* **509**, 143–147 (2011).
12. Shahrokhi, M., Mortazavi, B. & Berdiyorov, G. R. New two-dimensional boron nitride allotropes with attractive electronic and optical properties. *Solid State Communications* **253**, 51–56 (2017).
13. Kim, K. K. et al. Synthesis and characterization of hexagonal boron nitride film as a dielectric layer for graphene devices. *ACS nano* **6**, 8583–8590 (2012).
14. Zhang, X. et al. Structural and mechanical properties of monolayer amorphous carbon and boron nitride. *Physical Review B* **109**, 174106 (2024).
15. Li, J., Fan, X., Wei, Y. & Chen, G. Penta-bxny sheet: a density functional theory study of two-dimensional material. *Scientific reports* **6**, 1–9 (2016).
16. Yong, Y. et al. Ultrahigh capacity and reversible hydrogen storage media based on li-decorated t-bn monolayers. *Journal of Energy Storage* **72**, 108169 (2023).
17. Takahashi, L. & Takahashi, K. Structural stability and electronic properties of an octagonal allotrope of two dimensional boron nitride. *Dalton Transactions* **46**, 4259–4264 (2017).
18. Pontes, J. & Azevedo, S. Structural, electronic, and optical properties of the pai-bn monolayer: A first-principles study. *Chemical Physics Impact* **4**, 100074 (2022).
19. Lopes Lima, K., Lopes Mendonça, F., Giozza, W. F., de Sousa Júnior, R. T. & Ribeiro Junior, L. Insights into the dhq-bn: mechanical, electronic, and optical properties. *Scientific Reports* **14**, 2510 (2024).
20. Yu, L. *et al.* The synergistic modulation of electronic and geometry structures leads to ultra-low thermal conductivity of graphene-like borides (g-b3x5, x= n, p, as). arXiv preprint arXiv:2202.03622 (2022).
21. Monteiro, F., Lima, K. & Junior, L. A. R. Predicting Ψ-bn: Computational insights into its mechanical, electronic, and optical characteristics. *Computational Condensed Matter* **37**, e00853 (2023).
22. Wang, Z. et al. Phagraphene: a low-energy graphene allotrope composed of 5-6-7 carbon rings with distorted dirac cones. *Nano letters* **15**, 6182–6186 (2015).
23. Pontes, J., Frazão, N., Azevedo, D. L. & Lima, J. R. Electronic, optical, vibrational and thermodynamic properties of phabn structure: A first principles study. *Computational Materials Science* **188**, 110210 (2021).
24. Fan, Q. et al. Nanoribbons with nonalternant topology from fusion of polyazulene: carbon allotropes beyond graphene. *Journal of the American Chemical Society* **141**, 17713–17720 (2019).
25. Monteiro, F. et al. On the mechanical, electronic, and optical properties of the boron nitride analog for the recently synthesized biphenylene network: a dft study. *Journal of Molecular Modeling* **29**, 215 (2023).
26. Fan, Q. et al. Biphenylene network: A nonbenzenoid carbon allotrope. *Science* **372**, 852–856 (2021).
27. Enyashin, A. N. & Ivanovskii, A. L. *Graphene allotropes. physica status solidi (b)* **248**, 1879–1883 (2011).
28. Júnior, M. P. & Junior, L. R. Irida-graphene: A new 2d carbon allotrope. *FlatChem* **37**, 100469 (2023).
29. Zhang, Y.-F. & Guo, J. Li-decorated 2d irida-graphene as a potential hydrogen storage material: A dispersion-corrected density functional theory calculations. *International Journal of Hydrogen Energy* **50**, 1004–1014 (2024).
30. Tan, Y., Tao, X., Ouyang, Y. & Peng, Q. Stable and 7.7 wt% hydrogen storage capacity of ti decorated irida-graphene from first-principles calculations. *International Journal of Hydrogen Energy* **50**, 738–748 (2024).
31. Majidi, R. Irida-graphyne: A promising material for optoelectronic applications. *Materials Today Communications* **38**, 107641 (2024).
32. Felix, I. M. *et al.* Irida-graphene phonon thermal transport via non-equilibrium molecular dynamics simulations. *Nanoscale* (2024).
33. Duan, Z. et al. Reversible hydrogen storage with na-modified irida-graphene: A density functional theory study. *International Journal of Hydrogen Energy* **85**, 1–11 (2024).
34. Xiong, X., Cao, H.-B., Lu, Z., Liu, C.-S. & Ye, X.-J. Theoretical prediction on irida-graphene monolayer as promising anode material for lithium-ion batteries. *Computational Materials Science* **244**, 113225 (2024).
35. Yuan, L. et al. First-principles investigation of irida-graphene decorated with alkali metal for reversible hydrogen storage. *Computational and Theoretical Chemistry* **1239**, 114756 (2024).
36. Li, J. et al. Mechanics and crack analysis of irida graphene bilayer composite: A molecular dynamics study. *Journal of Composites Science* **7**, 490 (2023).
37. Bhattacharya, A., Bhattacharya, S. & Das, G. Band gap engineering by functionalization of bn sheet. *Physical Review B-Condensed Matter and Materials Physics* **85**, 035415 (2012).
38. Kaloni, T. P. & Mukherjee, S. Comparative study of electronic properties of graphite and hexagonal boron nitride (h-bn) using pseudopotential plane wave method. *Modern Physics Letters B* **25**, 1855–1866 (2011).
39. Haastrup, S. *et al.* The computational 2d materials database: high-throughput modeling and discovery of atomically thin crystals. *2D Materials* **5**, 042002 (2018).
40. Tignon, J. et al. From fermi's golden rule to the vacuum rabi splitting: Magnetopolaritons in a semiconductor optical microcavity. *Phys. Rev. Lett.* **74**, 3967. https://doi.org/10.1103/PhysRevLett.74.3967 (1995).
41. Kramers, H. A. La diffusion de la lumiere par les atomes. In *Atti del Congresso Internationale dei Fisici*, 1–13 (Como, Italy, 1927).
42. Kronig, R. d. L. On the theory of dispersion of X-rays. *J. Opt. Soc. Am.* **12**, 547–557, https://doi.org/10.1364/JOSA.12.000547 (1926).
43. Özçelik, V. O. & Ciraci, S. Size Dependence in the Stabilities and Electronic Properties of α-Graphyne and Its Boron Nitride Analogue. *The Journal of Physical Chemistry C* **117**, 2175–2182. https://doi.org/10.1021/jp3111869 (2013).
44. Topsakal, M., Cahangirov, S. & Ciraci, S. The response of mechanical and electronic properties of graphane to the elastic strain. *Applied Physics Letters* **96**, https://doi.org/10.1063/1.3353968 (2010). 0908.2887.
45. Majidi, R. Mechanical properties of novel forms of graphyne under strain: A density functional theory study. *Physica E: Low-Dimensional Systems and Nanostructures* **90**, 189–193. https://doi.org/10.1016/j.physe.2017.04.001 (2017).
46. Asadpour, M., Malakpour, S., Faghihnasiri, M. & Taghipour, B. Mechanical properties of two-dimensional graphyne sheet, analogous system of BN sheet and graphyne-like BN sheet. *Solid State Communications* **212**, 46–52. https://doi.org/10.1016/j.ssc.2015.02.005 (2015).
47. Kang, J., Li, J., Wu, F., Li, S. S. & Xia, J. B. Elastic, electronic, and optical properties of two-dimensional graphyne sheet. *Journal of Physical Chemistry C* **115**, 20466–20470. https://doi.org/10.1021/jp206751m (2011).
48. Maździarz, M. Comment on 'the computational 2d materials database: high-throughput modeling and discovery of atomically thin crystals'. *2D Materials* **6**, 048001 (2019).
49. Kohn, W. & Sham, L. J. Self-consistent equations including exchange and correlation effects. *Phys. Rev.* **140**, A1133–A1138. https://doi.org/10.1103/PhysRev.140.A1133 (1965).

50. Sánchez-Portal, D., Ordejón, P., Artacho, E. & Soler, J. M. Density-functional method for very large systems with lcao basis sets. *International Journal of Quantum Chemistry* **65**, 453–461. https://doi.org/10.1002/(SICI)1097-461X(1997)65:5<453::AID-QUA9>3.0.CO;2-V (1997).
51. Soler, J. M. et al. The SIESTA method for ab initio order- N materials simulation. *Journal of Physics: Condensed Matter* **14**, 2745–2779. https://doi.org/10.1088/0953-8984/14/11/302 (2002).
52. García, A. *et al.* Siesta: Recent developments and applications. *The Journal of chemical physics* **152** (2020).
53. Perdew, J. P., Burke, K. & Ernzerhof, M. Generalized gradient approximation made simple. *Phys. Rev. Lett.* **77**, 3865–3868. https://doi.org/10.1103/PhysRevLett.77.3865 (1996).
54. Heyd, J., Scuseria, G. E. & Ernzerhof, M. Hybrid functionals based on a screened Coulomb potential. *The Journal of Chemical Physics* **118**, 8207–8215. https://doi.org/10.1063/1.1564060 (2003).
55. Qin, X., Shang, H., Xiang, H., Li, Z. & Yang, J. HONPAS: A linear scaling open-source solution for large system simulations. *International Journal of Quantum Chemistry* **115**, 647–655. https://doi.org/10.1002/qua.24837 (2015).
56. Shang, H. et al. The dynamic parallel distribution algorithm for hybrid density-functional calculations in HONPAS package. *Computer Physics Communications* **254**, 107204. https://doi.org/10.1016/j.cpc.2020.107204 (2020).
57. Troullier, N. & Martins, J. L. Efficient pseudopotentials for plane-wave calculations. *Phys. Rev. B* **43**, 1993–2006. https://doi.org/10.1103/PhysRevB.43.1993 (1991).
58. Kleinman, L. & Bylander, D. M. Efficacious form for model pseudopotentials. *Phys. Rev. Lett.* **48**, 1425–1428. https://doi.org/10.1103/PhysRevLett.48.1425 (1982).
59. Monkhorst, H. J. & Pack, J. D. Special points for brillouin-zone integrations. *Phys. Rev. B* **13**, 5188–5192. https://doi.org/10.1103/PhysRevB.13.5188 (1976).

Acknowledgements

M.L.P.J. acknowledges the financial support of the FAP-DF grant 00193-00001807/2023-16. M.L.P.J. and L.A.R.J. thanks also to CENAPAD-SP (National High-Performance Center in São Paulo, State University of Campinas – UNICAMP, projects: proj960 and proj634, respectively) and NACAD (High-Performance Computing Center, Lobo Carneiro Supercomputer, Federal University of Rio de Janeiro – UFRJ, projects: a22002 and a22003, respectively) for the computational support provided. The authors acknowledge the National Laboratory for Scientific Computing (LNCC/MCTI, Brazil) for providing HPC resources for the SDumont supercomputer, contributing to the research results reported in this paper. This work received partial support from Brazilian agencies CAPES, CNPq, and FAPDF. L.A.R.J. acknowledges the financial support from FAP-DF grants 00193.00001808/2022-71 and 00193-00001857/2023-95, FAPDF-PRONEM grant 00193.00001247/2021-20, PDPG-FAPDF-CAPES Centro-Oeste 00193-00000867/2024-94, and CNPq grants 350176/2022-1 and 167745/2023-9.

Author contributions

M.L.P.J.: Data curation, Conceptualization, Formal analysis, Investigation, Writing - Review & Editing, Project administration, Funding acquisition. D.S.G.: Data curation, Software, Visualization. K.A.L.L.: Software, Investigation, Writing - Original Draft. F.L.L.M.: Investigation, Methodology, Writing - Original Draft, Funding acquisition. G.D.A.N.: Investigation, Validation, Writing - Original Draft, Funding acquisition. L.A.R.J.: Conceptualization, Validation, Investigation, Writing - Original Draft, Project administration, Supervision, Funding acquisition.

Declarations

Competing interests

The authors declare no competing interests.

Additional information

Supplementary Information The online version contains supplementary material available at https://doi.org/10.1038/s41598-024-79823-z.

Correspondence and requests for materials should be addressed to M.L.P.

Reprints and permissions information is available at www.nature.com/reprints.

Publisher's note Springer Nature remains neutral with regard to jurisdictional claims in published maps and institutional affiliations.

Open Access This article is licensed under a Creative Commons Attribution-NonCommercial-NoDerivatives 4.0 International License, which permits any non-commercial use, sharing, distribution and reproduction in any medium or format, as long as you give appropriate credit to the original author(s) and the source, provide a link to the Creative Commons licence, and indicate if you modified the licensed material. You do not have permission under this licence to share adapted material derived from this article or parts of it. The images or other third party material in this article are included in the article's Creative Commons licence, unless indicated otherwise in a credit line to the material. If material is not included in the article's Creative Commons licence and your intended use is not permitted by statutory regulation or exceeds the permitted use, you will need to obtain permission directly from the copyright holder. To view a copy of this licence, visit http://creativecommons.org/licenses/by-nc-nd/4.0/.

© The Author(s) 2024